



# Hybrid-mixed shell quadrilateral that allows for large solution steps and is low-sensitive to mesh distortion

Marko Lavrenčič<sup>1</sup> · Boštjan Brank<sup>1</sup>

Received: 19 March 2019 / Accepted: 16 August 2019 / Published online: 4 September 2019  
© Springer-Verlag GmbH Germany, part of Springer Nature 2019

## Abstract

We compare three nearly optimal quadrilateral finite elements for geometrically exact inextensible-director shell model. Two of them are revisited and one is novel. The assumed natural strain (ANS) element of Ko et al. (Comput Struct 185:1–14, 2017) shows low sensitivity to mesh distortion and excellent convergence behavior for most types of shell problems. The Hu–Washizu element with ANS shear strains of Wagner and Gruttmann (Int J Numer Methods Eng, 64:635–666, 2005) allows for large solution steps and is computationally fast. However, both formulations have undesirable weak spots, which we clearly identify by a comprehensive set of numerical examples. We show that a straightforward combination of both formulations results in a novel element that synergizes the positive features and eliminates the weak spots of its predecessors.

**Keywords** Nonlinear shells · Quadrilateral element · Assumed natural strain · Hybrid-mixed formulation · Mesh distortion · Large solution steps · Mesh-distortion sensitivity

## 1 Introduction

Development of a low-order (4-node) “optimal” nonlinear shell finite element is of great practical interest. Such an element should: (i) pass the basic tests; (ii) show nearly optimal convergence behavior; (iii) display low sensitivity to mesh distortion; (iv) allow for large solution steps, and (v) be computationally fast. It should maintain these favorable properties irrespective of the type of shell problem categorized by geometry, loading and boundary conditions. It is understood that it should be equipped with efficient description of large rotations.

Recently, Ko et al. [14] presented a 4-node shell finite element with the first three of the above listed favorable properties of the “optimal” shell finite element for most shell problem types. They called it “the new MITC4+” (hereinafter called MITC4+). The element is an extension of the nonlinear version of popular MITC4 (mixed interpolation of tensorial components) [7]. MITC4+ applies the assumed natural strain (ANS) concept also for the membrane strains. The latter relies on a combination and improvement of proposals from [4, 17]

performed by Ko et al. in [13, 14]. Numerical examples in [13–15] and our numerical experiments demonstrate that MITC4+ shows nearly optimal rate of convergence (also for nonlinear problems), and displays incredibly little sensitivity to mesh distortion. However, its weak spots are: (i) pure membrane (i.e. in-plane) deformations, and (ii) very large bending deformations accompanied by small membrane deformations (such problem is, e.g., deployable ring presented in section with numerical examples). In these cases, the ANS enhancement of the membrane behavior has only a minor effect, which is revealed by practically identical behavior of MITC4+ and MITC4. Thus, for the two mentioned shell problem types, MITC4+ does not remove membrane locking.

Wagner and Gruttmann [25] proposed a hybrid-mixed Hu–Washizu type nonlinear 4-node shell element that has the last two (plus the first one) of the above listed favorable properties of the “optimal” shell finite element; hereinafter, let us call it HW. HW interpolates independently displacements and rotations, all shell strains, and all shell internal forces. On the top, it applies the ANS [7] for the transverse shear strains. Numerical examples in [25] and our numerical experiments show that HW is very fast, can use large solution steps, and has good convergence behavior for regular meshes. However, it is sensitive to mesh distortion, which is its weak spot. It does not remove the membrane locking for distorted meshes.

✉ Boštjan Brank  
bbrank@fgg.uni-lj.si

<sup>1</sup> Faculty of Civil and Geodetic Engineering, University of Ljubljana, Jamova c. 2, 1000 Ljubljana, Slovenia

The aim of the present work is to present novel element that synergizes the positive features of MITC4+ and HW and eliminates their weak spots. It turns out that this can be achieved by a straightforward modification of HW [25] to include the ANS membrane strains [14]. Let us call the resulting element +HW. Our extensive numerical tests, partly presented in Sect. 4, demonstrate that +HW possesses all five above listed favorable properties of the “optimal” shell finite element. The weak spots of MITC4+ and HW are not present in +HW.

The rest of the paper is structured in the following way. Our version of the geometrically exact, inextensible-director shell model is summarized in Sect. 2. The interpolations for MITC4+, HW and +HW elements are presented in Sect. 3. In Sect. 4, performances of MITC4, MITC4+, HW and +HW are evaluated and compared, and conclusions are drawn in Sect. 5.

## 2 Shell model

### 2.1 Theory

We adopt the inextensible-director shell model with the Reissner–Mindlin kinematics, the detailed description of which is given in seminal work [22, 23], and many later works, see, e.g., [2, 3, 6, 11, 17, 25, 26] and references therein (among many others).

The position vectors at the initial and deformed configurations are the following functions of convected curvilinear coordinates  $\xi^1, \xi^2, \xi^3$ :

$$\mathbf{X}(\xi^1, \xi^2, \xi^3) = \mathbf{X}_0(\xi^1, \xi^2) + \xi^3 \mathbf{D}(\xi^1, \xi^2), \quad \xi^3 \in [-t/2, t/2], \tag{1}$$

$$\mathbf{x}(\xi^1, \xi^2, \xi^3) = \mathbf{x}_0(\xi^1, \xi^2) + \xi^3 \mathbf{d}(\xi^1, \xi^2), \tag{2}$$

respectively. The surface at  $\xi^3 = 0$  is called mid-surface. In what follows, we will omit writing the dependence of (scalar and vector) functions and functionals on curvilinear coordinates. In (1) and (2),  $\mathbf{D}$  is unit normal vector to the initial mid-surface that is called shell director,  $\mathbf{d} = \mathbf{d}(\boldsymbol{\vartheta})$  is rotated shell director (thus,  $\|\mathbf{D}\| = \|\mathbf{d}\| = 1$ ) described with rotation parameters  $\boldsymbol{\vartheta}$ ,  $t$  is initial shell thickness, and  $\mathbf{x}_0 = \mathbf{X}_0 + \mathbf{u}$ , where  $\mathbf{u}$  is mid-surface displacements. The “in-plane” covariant components of the Green–Lagrange strain tensor, which are expressed with respect to the contravariant base vectors at the point of initial mid-surface, are

$$E_{\alpha\beta} = \frac{1}{2}(\mathbf{x}_{,\alpha} \cdot \mathbf{x}_{,\beta} - \mathbf{X}_{,\alpha} \cdot \mathbf{X}_{,\beta}) = \varepsilon_{\alpha\beta} + \xi^3 \kappa_{\alpha\beta} + (\xi^3)^2 \rho_{\alpha\beta}, \quad \alpha, \beta \in \{1, 2\}, \tag{3}$$

where  $(\cdot)_{,\alpha}$  denotes  $\partial(\cdot)/\partial\xi^\alpha$ . The covariant components of the transverse shear strains are

$$E_{\alpha 3} = E_{3\alpha} = \frac{1}{2}(\mathbf{x}_{,\alpha} \cdot \mathbf{d} - \mathbf{X}_{,\alpha} \cdot \mathbf{D}) = \varepsilon_{\alpha 3} + \xi^3 \kappa_{\alpha 3}. \tag{4}$$

It is reasonable to neglect  $\rho_{\alpha\beta}$  in (3) and  $\kappa_{\alpha 3}$  in (4) because they have negligible effect on results, see, e.g., [22, 23] (this was also confirmed by our numerical testing). Moreover, it is convenient to define at the considered point of initial mid-surface a local Cartesian basis  $\{\hat{\mathbf{e}}_1, \hat{\mathbf{e}}_2, \hat{\mathbf{e}}_3 \equiv \mathbf{D}\}$ , and transform the covariant strain components to the (physical) Cartesian strain components. By adopting a Voigt notation, the resulting Cartesian membrane, bending and transverse shear strains (that depend on  $\mathbf{u}$  and  $\mathbf{d}$ ) are collected into three vectors,  $\boldsymbol{\varepsilon} = [\hat{\varepsilon}_{11}, \hat{\varepsilon}_{22}, 2\hat{\varepsilon}_{12}]^T$ ,  $\boldsymbol{\kappa} = [\hat{\kappa}_{11}, \hat{\kappa}_{22}, 2\hat{\kappa}_{12}]^T$  and  $\boldsymbol{\gamma} = [2\hat{\gamma}_{13}, 2\hat{\gamma}_{23}]^T$ , respectively.

We will adopt the Saint–Venant–Kirchhoff shell material model. The constitutive second Piola–Kirchhoff shell stress resultants at the mid-surface point under consideration are also defined in the local Cartesian basis and grouped into vectors of membrane forces, bending moments, and transverse shear forces as  $\mathbf{N} = [\hat{N}_{11}, \hat{N}_{22}, \hat{N}_{12}]^T$ ,  $\mathbf{M} = [\hat{M}_{11}, \hat{M}_{22}, \hat{M}_{12}]^T$  and  $\mathbf{Q} = [\hat{Q}_{13}, \hat{Q}_{23}]^T$ , respectively. The following relations apply:  $\mathbf{N} = \mathbf{C}^m \boldsymbol{\varepsilon}$ ,  $\mathbf{M} = \mathbf{C}^b \boldsymbol{\kappa}$ ,  $\mathbf{Q} = \mathbf{C}^s \boldsymbol{\gamma}$ , where  $\mathbf{C}^m$ ,  $\mathbf{C}^b$  and  $\mathbf{C}^s$  are the standard constitutive matrices for the inextensible-director shell model, which can be found, e.g., in [3]. Let the shell be loaded by (mid-surface) pressure and body loads, which are both included in  $\bar{\mathbf{b}}$ , and boundary forces  $\bar{\mathbf{t}}$ . For this type of loading, the potential energy functional reads as

$$\begin{aligned} \Pi(\mathbf{u}, \mathbf{d}) &= \Pi_{\text{int}}(\mathbf{u}, \mathbf{d}) - \Pi_{\text{ext}}(\mathbf{u}, \mathbf{d}) \\ &= \int_M \frac{1}{2}(\boldsymbol{\varepsilon} \cdot \mathbf{C}^m \boldsymbol{\varepsilon} + \boldsymbol{\kappa} \cdot \mathbf{C}^b \boldsymbol{\kappa} + \boldsymbol{\gamma} \cdot \mathbf{C}^s \boldsymbol{\gamma}) dA \\ &\quad - \left( \int_M \mathbf{u} \cdot \bar{\mathbf{b}} dA + \int_{\Gamma_i} \mathbf{u} \cdot \bar{\mathbf{t}} ds \right), \end{aligned} \tag{5}$$

where  $M$  is shell’s initial mid-surface, and  $\Gamma_i$  is part of the shell’s boundary with prescribed forces. The shell is in equilibrium when the potential energy functional is at its minimum. The necessary condition is

$$\begin{aligned} \delta\Pi(\mathbf{u}, \mathbf{d}; \delta\mathbf{u}, \delta\boldsymbol{\vartheta}_I) &= \int_M (\delta\boldsymbol{\varepsilon} \cdot \mathbf{N} + \delta\boldsymbol{\kappa} \cdot \mathbf{M} + \delta\boldsymbol{\gamma} \cdot \mathbf{Q}) dA \\ &\quad - \delta\Pi_{\text{ext}}(\delta\mathbf{u}, \delta\boldsymbol{\vartheta}) = 0, \end{aligned} \tag{6}$$

where  $\delta\Pi$  is variation of potential energy, formally obtained as  $\delta\Pi = \frac{d}{d\omega} \Pi(\mathbf{u} + \omega\delta\mathbf{u}, \boldsymbol{\vartheta} + \omega\delta\boldsymbol{\vartheta})|_{\omega=0}$ , where  $\omega$  is a scalar parameter,  $\delta\mathbf{u}$  and  $\delta\boldsymbol{\vartheta}$  are kinematically admissible variations of displacements and rotation parameters,  $\delta\boldsymbol{\varepsilon}$ ,  $\delta\boldsymbol{\kappa}$  and  $\delta\boldsymbol{\gamma}$  are vectors of virtual membrane, bending and transverse shear

strains, respectively, and  $\delta\Pi_{\text{ext}}$  is virtual work of external loading.

Either Eq. (5) or (6) is the starting point for the finite element discretization that completely relies on the interpolations of  $\mathbf{u}$  and  $\mathbf{d}$  and their variations. As a result, a displacement-based formulation is obtained, which, however, is not acceptable because it suffers from severe transverse shear locking and also from membrane locking.

### 2.2 Implementation for quadrilateral

Let  $M$  be discretized by  $n_{el}$  non-overlapping isoparametric 4 node finite elements, such that  $M \approx \bigcup_{e=1}^{n_{el}} A_e$ . Over the element, the mid-surface and shell director are interpolated as

$$\mathbf{X}_0^h(\xi, \eta) = \sum_{a=1}^4 N_a(\xi, \eta) \mathbf{X}_{0a}, \quad \tilde{\mathbf{D}}^h = \sum_{a=1}^{n_s} N_a(\xi, \eta) \mathbf{D}_a, \quad \mathbf{D}^h = \frac{\tilde{\mathbf{D}}^h}{\|\tilde{\mathbf{D}}^h\|}, \tag{7}$$

where subscript  $h$  denotes the approximation of a function of functional of the continuous shell model. In (7),  $(\cdot)_a$  are nodal values,  $\xi, \eta$  are convected isoparametric coordinates interpreted as  $\xi = \xi^1$  and  $\eta = \xi^2$  over  $A_e$ , and  $N_a(\xi, \eta)$  are bilinear Lagrange interpolation functions defined over the bi-unit square  $\mathcal{A}_e = [-1, 1] \times [-1, 1]$ . Moreover,  $\mathbf{D}_a$  is the exact shell's mid-surface unit normal vector at node  $a$ . The deformed configuration of the element is approximated as

$$\mathbf{x}_0^h = \mathbf{X}_0^h + \mathbf{u}^h, \quad \mathbf{u}^h(\xi, \eta) = \sum_{a=1}^{n_u} N_a(\xi, \eta) \mathbf{u}_a, \quad \tilde{\mathbf{d}}^h = \sum_{a=1}^{n_d} N_a(\xi, \eta) \mathbf{d}_a(\vartheta_a), \quad \mathbf{d}^h = \frac{\tilde{\mathbf{d}}^h}{\|\tilde{\mathbf{d}}^h\|}. \tag{8}$$

After using (7) and (8) in the potential energy functional (5), the latter becomes an assembly of finite element contributions with nodal values (of displacements and rotations) as unknowns:

$$\Pi^h = \mathbb{A}_{e=1}^{n_{el}} \Pi^e(\mathbf{u}^h, \mathbf{d}^h). \tag{9}$$

Here,  $\mathbb{A}$  is the finite element method assembly operator, see, e.g., [1, 5, 12, 29]. Variation of (9), see (6), leads to the system on nonlinear equations.

Let  $G$  and  $C$  denote a Gauss point and element's center-point with the local Cartesian bases  $\hat{\mathbf{e}}_{G,i}$  and  $\hat{\mathbf{e}}_{C,i}$ , respectively, where

$$\hat{\mathbf{e}}_{G,3} = \frac{\mathbf{X}_{0,1}^{h,G} \times \mathbf{X}_{0,2}^{h,G}}{\|\mathbf{X}_{0,1}^{h,G} \times \mathbf{X}_{0,2}^{h,G}\|}, \quad \hat{\mathbf{e}}_{C,3} = \frac{\mathbf{X}_{0,1}^{h,C} \times \mathbf{X}_{0,2}^{h,C}}{\|\mathbf{X}_{0,1}^{h,C} \times \mathbf{X}_{0,2}^{h,C}\|}, \tag{10}$$

$\hat{\mathbf{e}}_1 \perp \hat{\mathbf{e}}_3$ , and  $\hat{\mathbf{e}}_2 = \hat{\mathbf{e}}_3 \times \hat{\mathbf{e}}_1$ , see Fig. 1. We can define matrices used in the transformation below. When performing the transformation of covariant or contravariant components to the Cartesian components at center-point, we apply

$$\mathbf{J}_C^C = \left[ \mathbf{J}_{C\alpha\beta}^C \right], \quad \mathbf{J}_{C\alpha\beta}^C = \mathbf{X}_{0,\alpha}^{h,C} \cdot \hat{\mathbf{e}}_{C,\beta}. \tag{11}$$

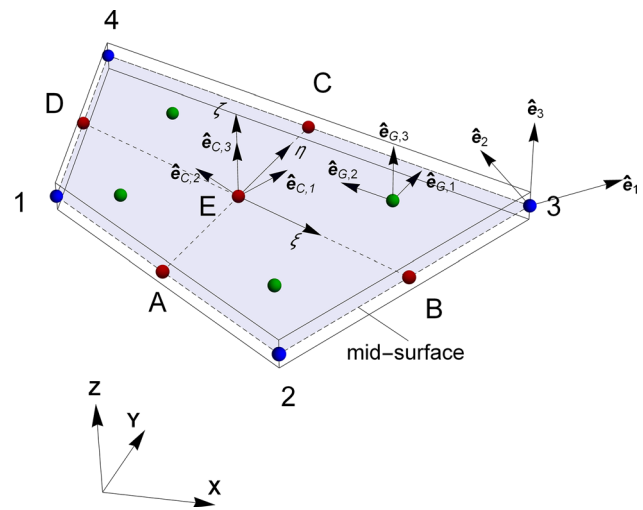


Fig. 1 Shell quadrilateral finite element: coordinate systems and ANS points

By replacing  $C$  by  $G$  in (11), one gets  $\mathbf{J}_G^G$  for the transformation of covariant or contravariant components to the Cartesian components at the Gauss point. One can also have

$$\mathbf{J}_C^G = \left[ \mathbf{J}_{C\alpha\beta}^G \right], \quad \mathbf{J}_{C\alpha\beta}^G = \mathbf{X}_{0,\alpha}^{h,G} \cdot \hat{\mathbf{e}}_{C,\beta}. \tag{12}$$

## 3 Nearly optimal shell finite elements

### 3.1 Assumed natural strain-based element

In this section, we briefly describe MITC4 and MITC4+ elements; for more details we refer to [7, 13, 14, 24], and references therein.

MITC4 applies the ANS concept for the transverse shear strains; the element's assumed covariant strains are

$$\begin{bmatrix} \tilde{\epsilon}_{13} \\ \tilde{\epsilon}_{23} \end{bmatrix} = \frac{1}{2} \begin{bmatrix} (1 - \eta)\epsilon_{13}^A + (1 + \eta)\epsilon_{13}^C \\ (1 - \xi)\epsilon_{23}^D + (1 + \xi)\epsilon_{23}^B \end{bmatrix}, \tag{13}$$

where A, B, C and D are mid-side points, see Fig. 1, at which the transverse shear strains are evaluated by using expression from Eq. (4)

$$\epsilon_{\alpha 3}^h = \frac{1}{2} \left( \mathbf{x}_{0,\alpha}^h \cdot \mathbf{d}^h - \mathbf{X}_{0,\alpha}^h \cdot \mathbf{D}^h \right), \tag{14}$$

and interpolations (7) and (8). The transformation of covariant strains (13) to the Cartesian strains at the Gauss point goes as

$$\left[ \widehat{\varepsilon}_{13}, \widehat{\varepsilon}_{23} \right]^T = \mathbf{J}_G^{G-1} \left[ \tilde{\varepsilon}_{13}, \tilde{\varepsilon}_{23} \right]^T. \tag{15}$$

The MITC4 change with respect to the displacement-based formulation is the replacement of vector  $\boldsymbol{\gamma}^h$  with  $\boldsymbol{\gamma}^{ANS} = \left[ 2\widehat{\varepsilon}_{13}, 2\widehat{\varepsilon}_{23} \right]^T$  in  $\Pi^e$ . Equation (9) becomes  $\mathbb{A}_{e=1}^{n_{el}} \Pi_{ANS}^e(\mathbf{u}^h, \mathbf{d}^h)$ , with element's contribution

$$\begin{aligned} \Pi_{ANS}^e(\mathbf{u}^h, \mathbf{d}^h) &= \int_{A_e} \frac{1}{2} (\boldsymbol{\varepsilon}^h \cdot \mathbf{C}^m \boldsymbol{\varepsilon}^h + \boldsymbol{\kappa}^h \cdot \mathbf{C}^b \boldsymbol{\kappa}^h + \boldsymbol{\gamma}^{ANS} \cdot \mathbf{C}^s \boldsymbol{\gamma}^{ANS}) dA \\ &\quad - \Pi_{ext}^e(\mathbf{u}^h, \mathbf{d}^h) \end{aligned} \tag{16}$$

integrated by 2x2 Gaussian quadrature.

The MITC4+ assumed covariant membrane strains are given as [14]

$$\begin{aligned} \tilde{\varepsilon}_{11} &= (-1 + \eta^2)(a_B \varepsilon_{11}^B + a_D \varepsilon_{11}^D + a_E \varepsilon_{12}^E) \\ &\quad + \frac{1}{2}(1 - 2a_A - \eta + 2a_A \eta^2) \varepsilon_{11}^A \\ &\quad + \frac{1}{2}(1 - 2a_C + \eta + 2a_C \eta^2) \varepsilon_{11}^C, \end{aligned} \tag{17}$$

$$\begin{aligned} \tilde{\varepsilon}_{22} &= (-1 + \xi^2)(a_A \varepsilon_{22}^A + a_C \varepsilon_{22}^C + a_E \varepsilon_{12}^E) \\ &\quad + \frac{1}{2}(1 - 2a_B + \xi + 2a_B \xi^2) \varepsilon_{22}^B \\ &\quad + \frac{1}{2}(1 - 2a_D - \xi + 2a_D \xi^2) \varepsilon_{22}^D, \end{aligned} \tag{18}$$

$$\begin{aligned} \tilde{\varepsilon}_{12} &= \frac{1}{4}(-\xi + 4a_A \xi \eta) \varepsilon_{11}^A + \frac{1}{4}(\xi + 4a_C \xi \eta) \varepsilon_{11}^C \\ &\quad + \frac{1}{4}(\eta + 4a_B \xi \eta) \varepsilon_{22}^B \\ &\quad + \frac{1}{4}(-\eta + 4a_D \xi \eta) \varepsilon_{22}^D + (1 + a_E \xi \eta) \varepsilon_{12}^E, \end{aligned} \tag{19}$$

where points A, B, C, D and E are shown in Fig. 1, and the strains at these points are evaluated by using expression from Eq. (3) as  $\varepsilon_{\alpha\beta}^h = 1/2(\mathbf{x}_{0,\alpha}^h \cdot \mathbf{x}_{0,\beta}^h - \mathbf{X}_{0,\alpha}^h \cdot \mathbf{X}_{0,\beta}^h)$ . Let us note that  $\tilde{\varepsilon}_{11}$  is quadratic in  $\eta$ ,  $\tilde{\varepsilon}_{22}$  is quadratic in  $\xi$ , and  $\tilde{\varepsilon}_{12}$  is a bilinear function. For the theoretical background of interpolations (17)–(19) and the related low-sensitivity to mesh distortion, we refer to [4, 13, 17]. The weighting factors that appear in (17)–(19) are

$$\begin{aligned} a_A &= \frac{c_\xi(c_\xi + 1)}{2d}, a_B = \frac{c_\eta(c_\eta - 1)}{2d}, a_C = \frac{c_\xi(c_\xi - 1)}{2d}, \\ a_D &= \frac{c_\eta(c_\eta + 1)}{2d}, a_E = \frac{2c_\xi c_\eta}{d}, \end{aligned} \tag{20}$$

where  $c_\xi, c_\eta$  and  $d$  measure element distortion

$$c_\xi = \mathbf{m}^\xi \cdot \mathbf{x}_d, c_\eta = \mathbf{m}^\eta \cdot \mathbf{x}_d, d = c_\xi^2 + c_\eta^2 - 1. \tag{21}$$

They are defined as (note that notations  $\mathbf{m}^\xi = \mathbf{m}^1, \mathbf{m}^\eta = \mathbf{m}^2, \mathbf{x}_\xi = \mathbf{x}_1$  and  $\mathbf{x}_\eta = \mathbf{x}_2$  are applied, and that  $\delta_\beta^\alpha$  is Kronecker's delta):

$$\begin{aligned} \mathbf{x}_d &= \frac{\partial^2 \mathbf{x}_0^h}{\partial \eta \partial \xi}, \quad \mathbf{m}^\alpha \cdot \mathbf{x}_\beta = \delta_\beta^\alpha, \quad \mathbf{m}^\alpha \cdot \mathbf{n} = 0, \\ \mathbf{x}_1 &= \left. \frac{\partial \mathbf{x}_0^h}{\partial \xi} \right|_{\eta=0}, \quad \mathbf{x}_2 = \left. \frac{\partial \mathbf{x}_0^h}{\partial \eta} \right|_{\xi=0}, \quad \mathbf{n} = \frac{\mathbf{x}_1 \times \mathbf{x}_2}{\|\mathbf{x}_1 \times \mathbf{x}_2\|}. \end{aligned} \tag{22}$$

The weighting factors in (20) are configuration dependent. In computations, they are updated at every solution increment. For solution increment  $n + 1$ , the converged configuration at solution increment  $n$  is used to compute vectors in (22) and constants in (20). An illustration of distortion vectors in (22) is given in Fig. 2.

The covariant membrane strains (17)–(19) are transformed to the Cartesian strains at the Gauss point as

$$\left[ \widehat{\varepsilon}_{11}, \widehat{\varepsilon}_{22}, 2\widehat{\varepsilon}_{12} \right]^T = \mathbf{T}_G^{G-1} \left[ \tilde{\varepsilon}_{11}, \tilde{\varepsilon}_{22}, 2\tilde{\varepsilon}_{12} \right]^T, \tag{23}$$

where the transformation matrix is

$$\mathbf{T}_G^G = \begin{bmatrix} (J_{G11}^G)^2 & (J_{G12}^G)^2 & J_{G11}^G J_{G12}^G \\ (J_{G21}^G)^2 & (J_{G22}^G)^2 & J_{G21}^G J_{G22}^G \\ 2J_{G11}^G J_{G21}^G & 2J_{G12}^G J_{G22}^G & J_{G11}^G J_{G22}^G + J_{G12}^G J_{G21}^G \end{bmatrix} \tag{24}$$

and  $\boldsymbol{\varepsilon}^{ANS} = \left[ \widehat{\varepsilon}_{11}, \widehat{\varepsilon}_{22}, 2\widehat{\varepsilon}_{12} \right]^T$ . Elements' contribution to the potential energy functional reads as

$$\begin{aligned} \Pi_{ANS+}^e(\mathbf{u}^h, \mathbf{d}^h) &= \int_{A_e} \frac{1}{2} (\boldsymbol{\varepsilon}^{ANS} \cdot \mathbf{C}^m \boldsymbol{\varepsilon}^{ANS} + \boldsymbol{\kappa}^h \cdot \mathbf{C}^b \boldsymbol{\kappa}^h + \boldsymbol{\gamma}^{ANS} \cdot \mathbf{C}^s \boldsymbol{\gamma}^{ANS}) dA \\ &\quad - \Pi_{ext}^e(\mathbf{u}^h, \mathbf{d}^h). \end{aligned} \tag{25}$$

### 3.2 Hybrid-mixed element

In this section, we briefly describe HW element; for more details we refer to [25].

Element's contribution to the Hu–Washizu functional is

$$\begin{aligned} \Pi_{HW}^e(\mathbf{u}^h, \mathbf{d}^h, \boldsymbol{\varepsilon}^{HW}, \boldsymbol{\sigma}^{HW}) &= \int_{A_e} \left[ \frac{1}{2} \boldsymbol{\varepsilon}^{HW} \cdot \mathbf{C} \boldsymbol{\varepsilon}^{HW} + \boldsymbol{\sigma}^{HW} \cdot (\boldsymbol{\varepsilon}^h - \boldsymbol{\varepsilon}^{HW}) \right] dA \\ &\quad - \Pi_{ext}^e(\mathbf{u}^h, \mathbf{d}^h), \end{aligned} \tag{26}$$

where the strains, stress resultants, and displacement-derived strains (all represented in Gauss points in local Cartesian bases) are

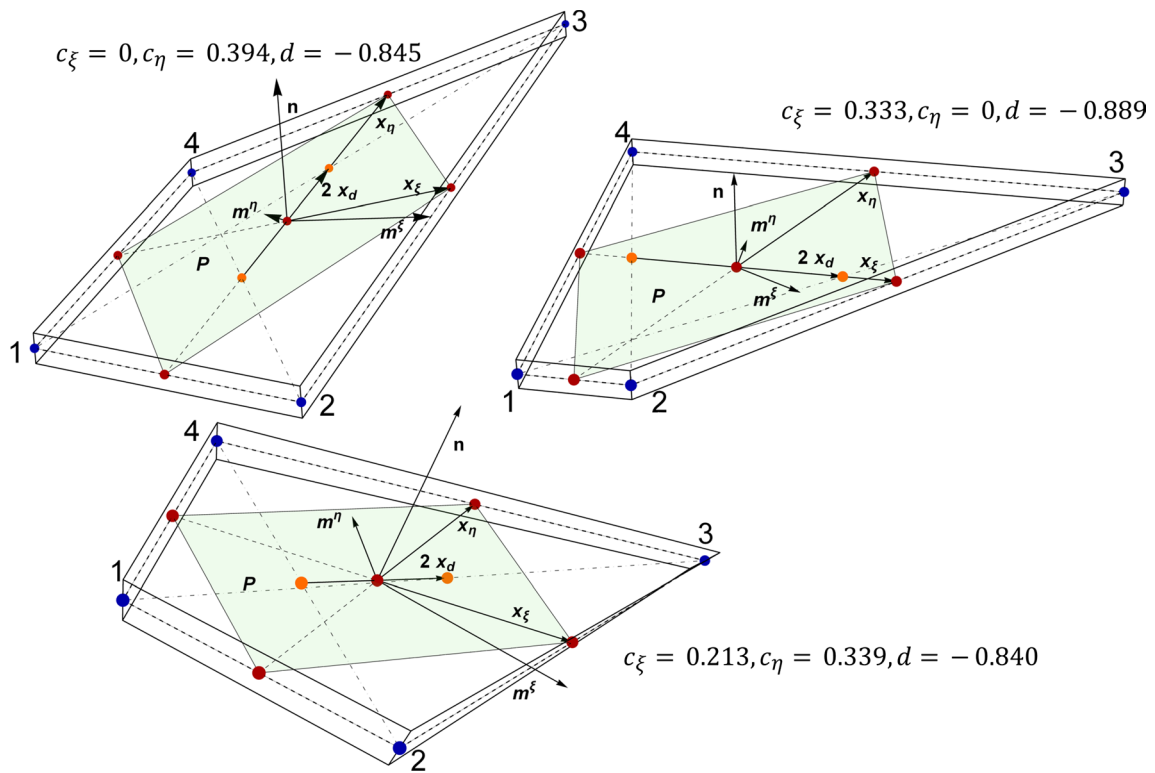


Fig. 2 Distortion vectors for two in-plane distortions (top) and out-of-plane distortion (bottom)

$$\epsilon^{HW} = [\epsilon^{HW,T}, \kappa^{HW,T}, \gamma^{HW,T}]^T, \sigma^{HW} = [N^{HW,T}, M^{HW,T}, Q^{HW,T}]^T, \tag{27}$$

$$\epsilon^h = [\epsilon^{h,T}, \kappa^{h,T}, \gamma^{h,T}]^T, \tag{28}$$

respectively, and  $C = \text{DIAG}[C^m, C^b, C^s]$ . The assembly is performed in a standard way as  $\Pi_{HW}^h = \mathbb{A}_{e=1}^{n_{el}} \Pi_{HW}^e$ . The performance of a hybrid-mixed shell element depends on the interpolations chosen for strains and stress resultants. For plane stress quadrilaterals, “optimal” stress interpolation was derived in [20] (see, e.g., [30] for the discussion on optimality). Because the membrane and bending relations of the applied shell model enforce the zero through-the-thickness normal stress constraint, these interpolations retain the same level of optimality if applied to membrane forces and bending moments of shell quadrilateral, as is the case in [25]:

$$\begin{bmatrix} \bar{n}^{11} \\ \bar{n}^{22} \\ \bar{n}^{12} \end{bmatrix} = \begin{bmatrix} \bar{\beta}_1 + (\eta - \bar{\eta})\bar{\beta}_9 \\ \bar{\beta}_2 + (\xi - \bar{\xi})\bar{\beta}_{10} \\ \bar{\beta}_3 \end{bmatrix}, \quad \begin{bmatrix} \bar{m}^{11} \\ \bar{m}^{22} \\ \bar{m}^{12} \end{bmatrix} = \begin{bmatrix} \bar{\beta}_4 + (\eta - \bar{\eta})\bar{\eta}\bar{\beta}_{11} \\ \bar{\beta}_5 + (\xi - \bar{\xi})\bar{\beta}_{12} \\ \bar{\beta}_6 \end{bmatrix}. \tag{29}$$

Here,  $\bar{\beta}$ -s are element’s stress resultant parameters, and  $\bar{\xi}$  and  $\bar{\eta}$  are coordinates of the center of gravity of the element. The interpolation for the contravariant components of the transverse shear forces may be chosen in the linear manner, see [25]:

$$\begin{bmatrix} \bar{q}^{13} \\ \bar{q}^{23} \end{bmatrix} = \begin{bmatrix} \bar{\beta}_7 + (\eta - \bar{\eta})\bar{\beta}_{13} \\ \bar{\beta}_8 + (\xi - \bar{\xi})\bar{\beta}_{14} \end{bmatrix}. \tag{30}$$

The contravariant stress resultant components (29) and (30) need to be transformed to the Cartesian components that enter  $\sigma^{HW}$  in (27). For the element to pass the patch-test, each stress resultant should have a constant part. This is achieved if the transformation is performed at one element’s point (and be considered valid for the whole element). For this purpose, the center-point is chosen, which leads to

$$\sigma^{HW} = N_\sigma \beta, \quad N_\sigma = [\mathbf{1}_{8 \times 8}, \mathbf{M}_\sigma], \quad \mathbf{M}_\sigma = \text{DIAG}[N_\sigma^m, N_\sigma^b, N_\sigma^s], \tag{31}$$

where  $\mathbf{1}_{8 \times 8}$  is unit matrix,  $\beta = [\beta_1, \dots, \beta_8, \bar{\beta}_9, \dots, \bar{\beta}_{14}]^T$  (note that the first 8 components of  $\beta$  differ from  $\bar{\beta}_1, \dots, \bar{\beta}_8$  in (29) due to the transformation), and

$$\mathbf{N}_\sigma^m = \mathbf{N}_\sigma^b = \begin{bmatrix} (\mathbf{J}_{C11}^C)^2(\eta - \bar{\eta}) & (\mathbf{J}_{C21}^C)^2(\xi - \bar{\xi}) \\ (\mathbf{J}_{C12}^C)^2(\eta - \bar{\eta}) & (\mathbf{J}_{C22}^C)^2(\xi - \bar{\xi}) \\ \mathbf{J}_{C11}^C \mathbf{J}_{C12}^C(\eta - \bar{\eta}) & \mathbf{J}_{C21}^C \mathbf{J}_{C22}^C(\xi - \bar{\xi}) \end{bmatrix}, \mathbf{N}_\sigma^s = \begin{bmatrix} \mathbf{J}_{C11}^C(\eta - \bar{\eta}) & \mathbf{J}_{C21}^C(\xi - \bar{\xi}) \\ \mathbf{J}_{C12}^C(\eta - \bar{\eta}) & \mathbf{J}_{C22}^C(\xi - \bar{\xi}) \end{bmatrix}. \tag{32}$$

In [25], identical interpolation as in (29) and (30) is chosen for the contravariant components of shell strains with  $\bar{\alpha}$ -s as element’s strain parameters. In order to keep the components of vectors in scalar products in (26) in the same basis, the transformation of contravariant strains to the Cartesian strains is again performed at element’s center-point as

$$\epsilon^{HW} = \mathbf{N}_\epsilon \boldsymbol{\alpha}, \mathbf{N}_\epsilon = [\mathbf{1}_{8 \times 8}, \mathbf{M}_\epsilon], \mathbf{M}_\epsilon = \text{DIAG}[\mathbf{N}_\epsilon^m, \mathbf{N}_\epsilon^b, \mathbf{N}_\epsilon^s], \tag{33}$$

where  $\mathbf{N}_\epsilon^s = \mathbf{N}_\sigma^s$ ,  $\mathbf{N}_\epsilon^m = \text{DIAG}[1, 1, 2]\mathbf{N}_\sigma^m$ ,  $\mathbf{N}_\epsilon^b = \text{DIAG}[1, 1, 2]\mathbf{N}_\sigma^b$ , and  $\boldsymbol{\alpha} = [\alpha_1, \dots, \alpha_8, \bar{\alpha}_9, \dots, \bar{\alpha}_{14}]^T$ . To retain the same pattern of transformation, and to keep the components of all vectors in (26) in the same basis, the displacement-derived strains are also transformed via center-point as:

$$\epsilon^h = \bar{\mathbf{N}}_\epsilon \boldsymbol{\chi}, \boldsymbol{\chi} = [\epsilon_{11}^h, \epsilon_{22}^h, 2\epsilon_{12}^h, \kappa_{11}^h, \kappa_{22}^h, 2\kappa_{12}^h, 2\epsilon_{13}^h, 2\epsilon_{23}^h]^T, \bar{\mathbf{N}}_\epsilon = \text{DIAG}[\mathbf{T}_C^C, \mathbf{T}_C^C, \mathbf{J}_C^C]^{-1}. \tag{34}$$

The authors of HW [25] replaced the last two components in  $\boldsymbol{\chi}$  by ANS interpolations  $2\tilde{\epsilon}_{13}$  and  $2\tilde{\epsilon}_{23}$  from (13) in order to treat better the transverse shear locking.

The stress resultant interpolations (29) can be considered as optimal ones, while the strain interpolations are just one of the possibilities. Other suitable interpolations may be applied (e.g., with more parameters or/and with covariant strain components), which, however, produce only minor changes in results according to [27, 28]. The changes in the interpolation of the displacement-derived strains  $\boldsymbol{\chi}$  in (34) have much larger influence.

The variation of  $\Pi_{HW}^h$  is  $\delta \Pi_{HW}^h = \frac{d}{d\omega} \Pi_{HW}^h(\mathbf{v} + \omega \delta \mathbf{v}, \boldsymbol{\alpha} + \omega \delta \boldsymbol{\alpha} + \boldsymbol{\beta} + \omega \delta \boldsymbol{\beta})|_{\omega=0}$ , where  $\omega$  is a scalar parameter,  $\mathbf{v}$  is vector of all nodal degrees of freedom, and  $\delta \mathbf{v}$ ,  $\delta \boldsymbol{\alpha}$  and  $\delta \boldsymbol{\beta}$  are admissible variations. The stationary point  $\delta \Pi_{HW}^h = 0$  yields three equations that need to be linearized in order to be solved iteratively. The condensation of iterative vectors  $\Delta \boldsymbol{\alpha}$  and  $\Delta \boldsymbol{\beta}$  is performed from linearized equations. Inversion due to condensation is possible for the sequence  $\{\Delta \boldsymbol{\alpha}, \Delta \boldsymbol{\beta}\}$  and it fails (due to singularity) if the vectors are interchanged. For implementation details we refer to [9, 10, 23, 25].

### 3.3 Modified hybrid-mixed element

+HW is a modified HW formulation [25] described in the previous section. Although the modification is minor, its effect is large, as shown in numerical examples below.

In particular, the displacement-derived membrane strains of HW are replaced by the ANS interpolation of strains. Thus, Eq. (34) is replaced by

$$\epsilon^{h+} = \bar{\mathbf{N}}_\epsilon^+ \boldsymbol{\chi}^+, \boldsymbol{\chi}^+ = [\tilde{\epsilon}_{11}, \tilde{\epsilon}_{22}, 2\tilde{\epsilon}_{12}, \kappa_{11}^h, \kappa_{22}^h, 2\kappa_{12}^h, 2\tilde{\epsilon}_{13}, 2\tilde{\epsilon}_{23}]^T, \bar{\mathbf{N}}_\epsilon^+ = \text{DIAG}[\mathbf{T}_C^G, \mathbf{T}_C^G, \mathbf{J}_C^G]^{-1}, \tag{35}$$

where the ANS strains, which are marked by  $\tilde{\cdot}$ , are given in (13) and (17)–(19). We adopt a transformation that relies on the components of  $\mathbf{J}_C^G$ , which are provided in (12), and matrix  $\mathbf{T}_C^G$ , which is obtained by using the components from (12) in place of those in (24).

In functional (26), the displacement-derived strains  $\epsilon^h$  are replaced by the strains  $\epsilon^{h+} = [\boldsymbol{\epsilon}^{ANS,T}, \boldsymbol{\kappa}^{h,T}, \boldsymbol{\gamma}^{ANS,T}]^T$  from (35), with the ANS strain vectors defined as given in

### Sect. 3.1

$$\Pi_{+HW}^e(\mathbf{u}^h, \mathbf{d}^h, \epsilon^{HW}, \boldsymbol{\sigma}^{HW}) = \int_{A_e} \left[ \frac{1}{2} \epsilon^{HW} \cdot \mathbf{C} \epsilon^{HW} + \boldsymbol{\sigma}^{HW} \cdot (\epsilon^{h+} - \epsilon^{HW}) \right] dA - \Pi_{\text{ext}}^e(\mathbf{u}^h, \mathbf{d}^h). \tag{36}$$

The interpolations of  $\epsilon^{HW}$  and  $\boldsymbol{\sigma}^{HW}$  remain the same as in Sect. 3.2.

## 4 Numerical examples

The presented shell formulations (MITC4, MITC4+, HW and +HW) were implemented into computer code AceFEM [16]. The last four numerical examples below were computed by the adaptive incremental load factor

$$\Delta \lambda_{\min} \leq \Delta \lambda = B(I_n) \Delta \lambda_n \leq \Delta \lambda_{\max}, B = \begin{cases} 2 - \left(\frac{I_n - 1}{I_o - 1}\right)^2, & I_n < I_o \\ 1 - \frac{1}{2} \left(\frac{I_n - I_o}{N - I_o}\right)^2, & I_n \geq I_o \end{cases} \tag{37}$$

**Table 1** Data for adaptive load factor procedure

Example	$\Delta \lambda_{\min}$	$\Delta \lambda_{\max}$	$\Delta \lambda_{\text{initial}}$
4.4	$10^{-8}$	$2 \times 10^{-2}$	$5 \times 10^{-2}$
4.5	$10^{-8}$	$5 \times 10^{-1}$	$1 \times 10^{-2}$
4.6	$10^{-8}$	$2 \times 10^{-12}$	$5 \times 10^{-2}$
4.7	$10^{-12}$	$10^{-4}$	$10^{-4}$

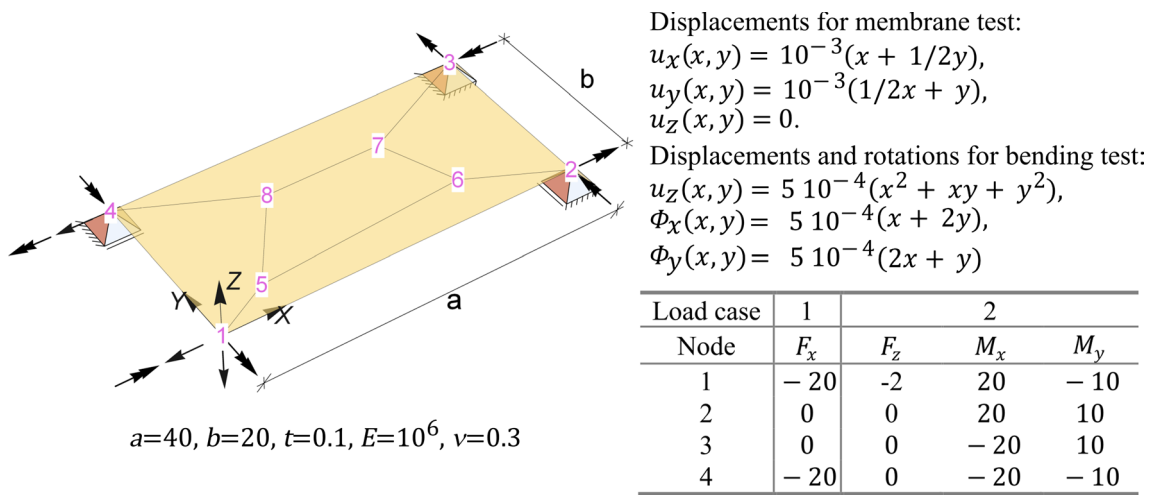


Fig. 3 Patch tests data

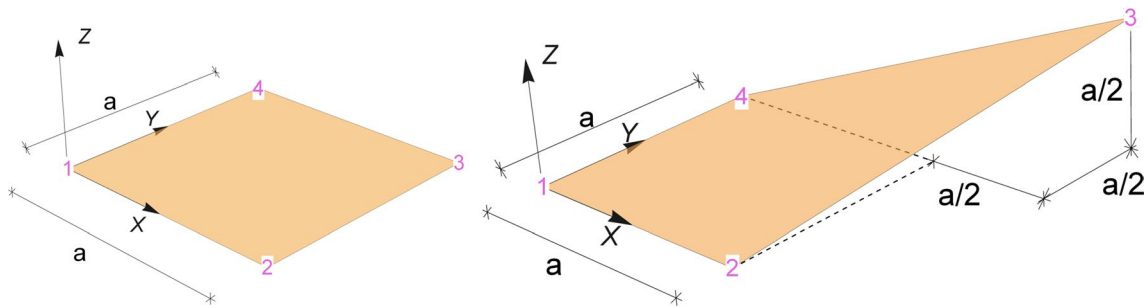


Fig. 4 Elements for eigenvalue analysis

Here,  $\Delta\lambda$  and  $\Delta\lambda_n$  are current and last incremental load factors, respectively;  $I_n$  is the number of iterations from the last increment; and  $I_0 = 8$  and  $N = 15$  are the numbers of desired and allowed incremental iterations, respectively. If

no convergence is reached in 15 iterations, the back-step is performed and the current increment is recomputed with  $\Delta\lambda/2$ . The values of the parameters are given in Table 1. The convergence tolerance was  $10^{-8}$ .

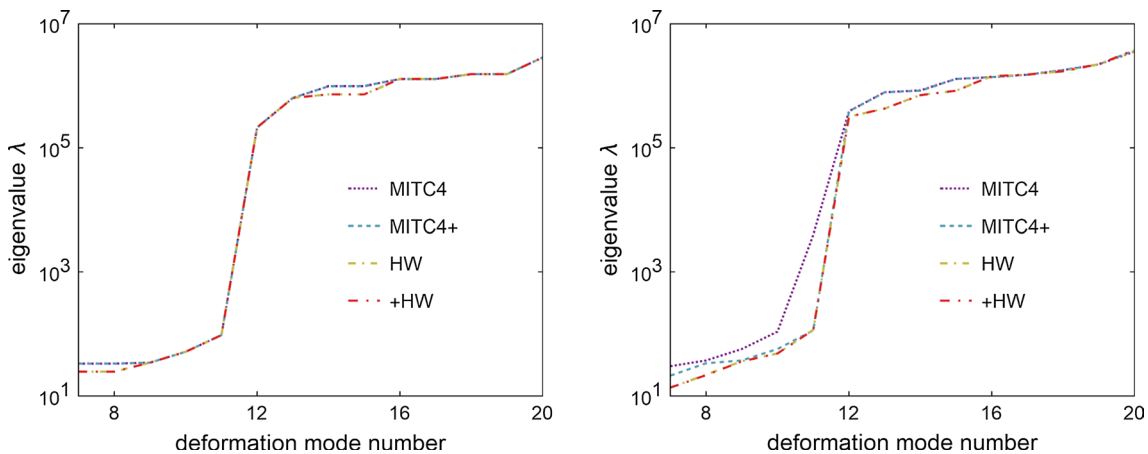
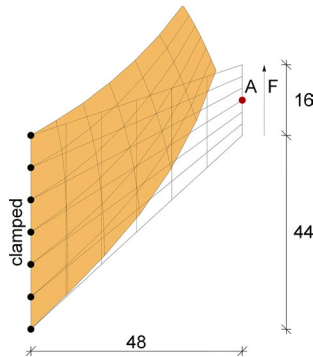


Fig. 5 Eigenvalues of square (left) and distorted (right) element

**Table 2** Stiffness matrix condition number

FE	Square element		Distorted element	
	$c \cdot 10^4$	$\frac{c}{c_{MITC4}}$	$c \cdot 10^4$	$\frac{c}{c_{MITC4}}$
MITC4	8.67	1.00	11.93	1.00
MITC4+ [14]	8.67	1.00	17.65	1.48
HW [25]	11.70	1.35	26.52	2.22
+HW	11.70	1.35	27.60	2.31



**Fig. 6** Cook's membrane: initial and deformed configuration (MITC4)

**4.1 Patch tests**

Two sets of patch tests were considered. The data for the first one are taken from [26]. Two arrangements of displacements and rotations are imposed at nodes 1–4 in accordance with formulae from Fig. 3. The exact solutions are constant membrane strains  $\epsilon_{xx} = \epsilon_{yy} = 2\epsilon_{xy} = 10^{-3}$  and constant curvatures  $\kappa_{xx} = \kappa_{yy} = \kappa_{xy} = -10^{-3}$ , respectively. Linear versions of all the formulations computed these exact values.

The data for the second set is taken from [25]. Two loading cases are imposed in accordance with table in Fig. 3. All formulations computed correct values of membrane forces  $n_{xx} = 2, n_{yy} = n_{xy} = 0$  for load case 1 and moments  $m_{xx} = m_{yy} = m_{xy} = 1$  for load case 2.

**4.2 Conditioning number**

We checked the conditioning number of the initial (i.e. linear) stiffness matrix for the derived formulations. To this end, we computed eigenvalues of stiffness matrix of a square element and distorted (curved) element, see Fig. 4, with  $a = 2, t = 0.02, E = 10^8, \nu = 0.3$ .

All the formulations have six zero eigenvalues corresponding to the six rigid body modes. The curves in Fig. 5 exhibit a jump at certain deformation mode number. Lower eigenvalues (before the jump) relate to the bending-dominated modes, and higher eigenvalues (after the jump) relate to the stiffer membrane- and shear-dominated modes. Figure 5 shows that for the lowest modes, HW and +HW have smaller eigenvalues than MITC4 and MITC4+. Thus, the former are more flexible for pure bending modes than the latter. The same is valid for the membrane modes just after the jump. Hence, HW and +HW are more flexible for lowest membrane-dominating modes than MITC4 and MITC4+. The distorted element displays pollution of MITC4 bending-dominated modes 7–11 by excessive membrane deformations, which is the reason why MITC4 curve departs from others in this region. Table 2 demonstrates that the condition number of the stiffness matrix  $c = \lambda_{max}/\lambda_{min}$  (here,  $\lambda$  is a non-zero eigenvalue) is of the same order for the considered formulations for both tests.

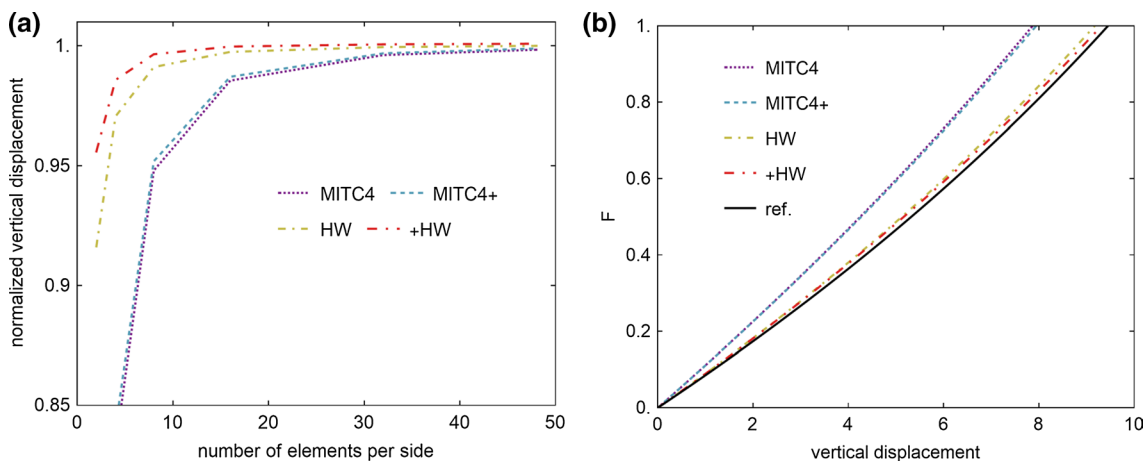


**Fig. 7** Cook's membrane: **a** convergence, **b** load versus displacement for 4×4 mesh

**Table 3** Cook’s membrane convergence: vertical displacement at  $F=1$

FE\mesh	2×2	4×4	8×8	16×16	32×32	48×48
MITC4	5.572	7.868	8.960	9.313	9.414	9.435
MITC4+ [14]	5.649	7.944	8.996	9.329	9.421	9.440
HW [25]	8.660	9.172	9.367	9.427	9.446	9.451
+HW	9.035	9.316	9.418	9.448	9.457	9.459

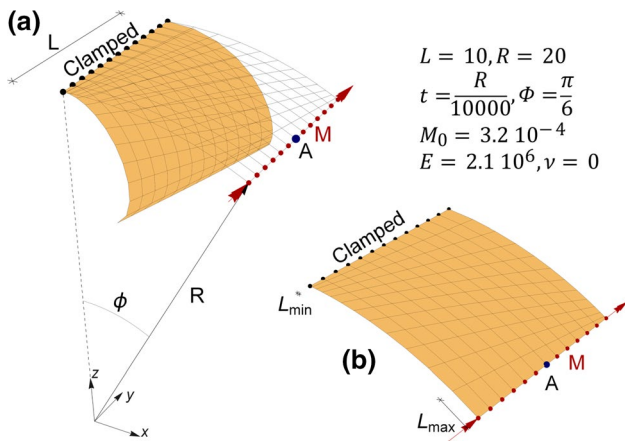


**Fig. 8** Cylindrical panel: **a** initial and final deformed configuration for regular mesh (MITC4); **b** distorted mesh

### 4.3 Cook’s membrane

We performed nonlinear analysis of Cook’s membrane, which is clamped at one end and subjected to uniformly distributed force  $F = F_0 \lambda$ , where  $F_0 = 1$  and  $\lambda$  is load factor, at the opposite end, see Fig. 6. The data are  $E = 2$ ,  $\nu = 1/3$  and thickness  $t = 1$ , as proposed in [21]. The load was applied in 10 increments. This is a pure membrane test that also incorporates element distortion. It primarily shows how well

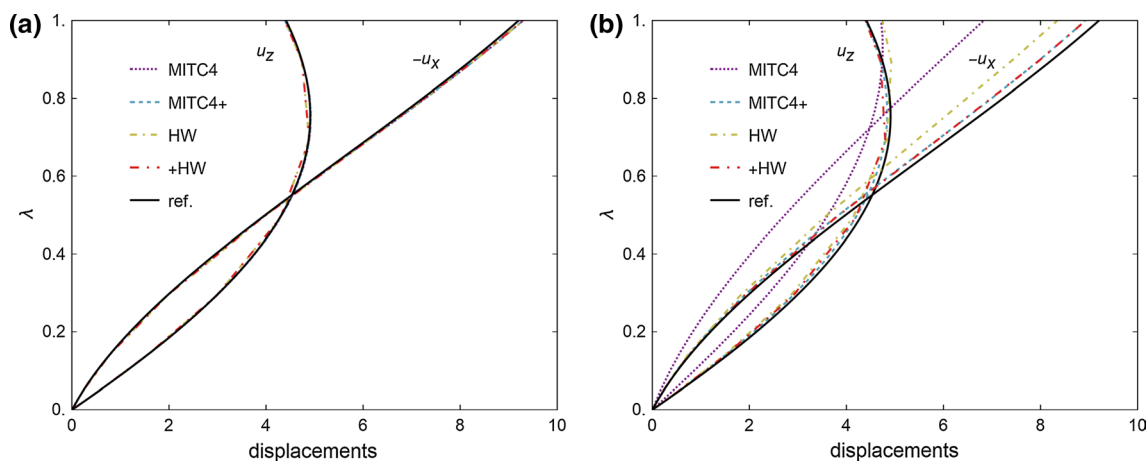
a formulation can handle the in-plane bending dominated by the shear.

Figure 7a shows the convergence of vertical displacement at point A for  $F = 1$ , normalized with respect to the reference solution, obtained by  $48 \times 48$  mesh of HW. Note that HW and +HW exhibit excellent convergence. On the other hand, the MITC4 and MITC4+ convergence is considerably worse; they require a fine mesh to converge (Table 3). Figure 7b shows vertical displacement at node A versus applied load for  $4 \times 4$  mesh. The HW and +HW formulations are already close to the reference one, while MITC4 and MITC4+ are much too stiff. The latter two almost match, which is because the membrane parts of the MITC4 and MITC4+ formulations differ only slightly for pure membrane problems, see also [13].

### 4.4 Cylindrical panel

Thin cylindrical panel, considered also in [14], is clamped at one edge and subjected to distributed moment  $M = \lambda M_0$  along the opposite edge, see Fig. 8. This is a pure bending test. Regular and distorted meshes shown in Fig. 8 are used; the ratio  $L_{min}/L_{max} = 1/12$ .

Figure 9 shows the applied load versus displacements  $u_z$  and  $-u_x$  of point A; the reference results obtained by regular mesh of  $48 \times 48$  HW elements match perfectly those obtained for  $32 \times 32$  regular mesh of MITC9 elements in



**Fig. 9** Cylindrical panel response for **a** regular mesh and **b** distorted mesh

**Table 4** Cylindrical panel: computational details for  $M = M_0$  for regular mesh (top) and distorted mesh (bottom);  $u_{x,ref} = -9.21$

FE	MITC4	MITC4+ [14]	HW [25]	+HW
Displacement $-u_x$ ( $\frac{-u_x}{-u_{x,ref}}$ [%])	9.30 (101)	9.30 (101)	9.30 (101)	9.30 (101)
Normalized CPU time	1.00	0.89	0.23	0.23
Req. no. of load increments	22	22	7	7
Number of total iterations	205	205	41	41
Number of back-steps	0	0	0	0
Displacement $-u_x$ ( $\frac{-u_x}{-u_{x,ref}}$ [%])	6.83 (74)	8.92 (97)	8.35 (91)	8.93 (97)
Normalized CPU time	1.00	0.95	0.19	0.33
Req. no. of load increments	22	35	7	7
Number of total iterations	220	370	41	41
Number of back-steps	1	1	0	0

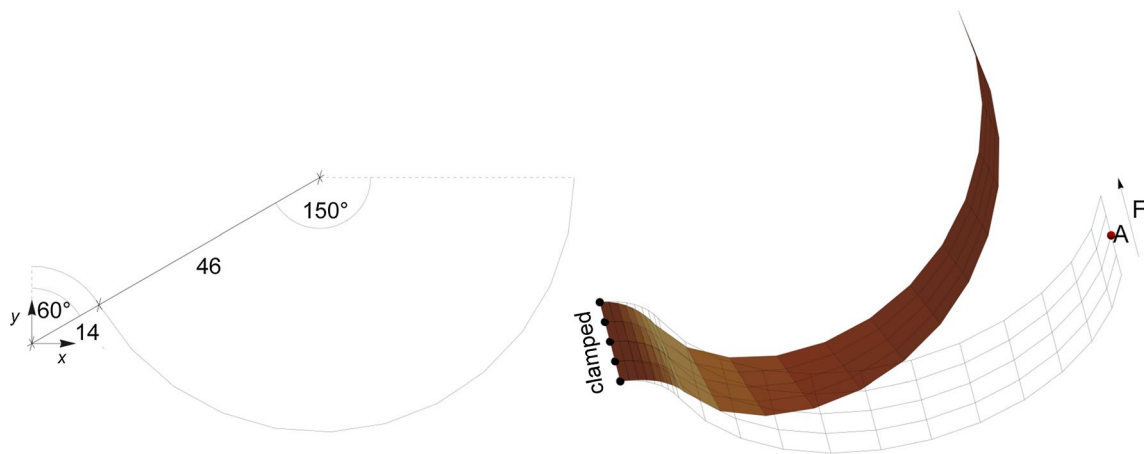


**Fig. 10** Raasch's hook: geometry (left); initial and deformed configurations (right)

[14]. The response of all formulations is practically the same for the regular mesh, see Fig. 9a. For the distorted mesh, see Fig. 9b, MITC4 is affected most, HW shows reasonable results, while MITC4+ and +HW give similar results as for the regular mesh. The results indicate that for membrane locking remedy in pure bending case, MITC4+ is more effective than the hybrid-mixed treatment. The robustness and speed of the formulations are compared in Table 4.

#### 4.5 Raasch's hook

Raasch's hook consists of two arches with different radii of curvature; see Fig. 10. It is clamped at one end and subjected to a uniformly distributed force  $F = \lambda F_0$  at the opposite end. The data thickness  $t = 0.02$ , width  $w = 20$ ,  $F_0 = 1$ ,  $E = 3300$  and  $\nu = 0.3$ , are taken after [14]. The shell was analyzed with a mesh of  $(2N + 3N) \times N$  elements, where  $N \in \{2, 4, 8, 16, 32\}$ . Here,  $N$  is the number of elements in the width, and  $2N$  and  $3N$  are numbers of elements for the first and second arch, respectively. In addition to regular meshes, we also used distorted meshes with pattern shown

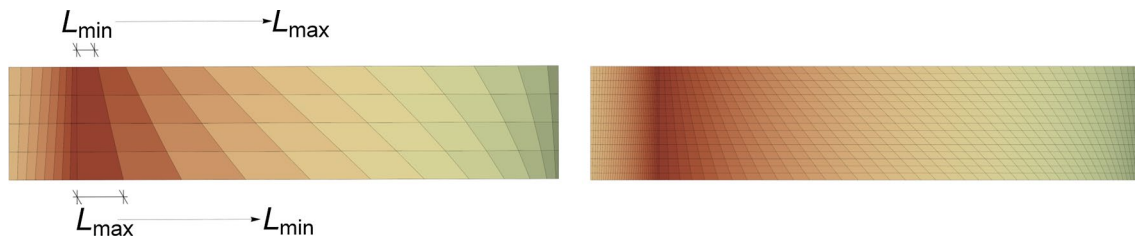


**Fig. 11** Raasch's hook: distorted meshes with  $N=4$  and  $N=16$

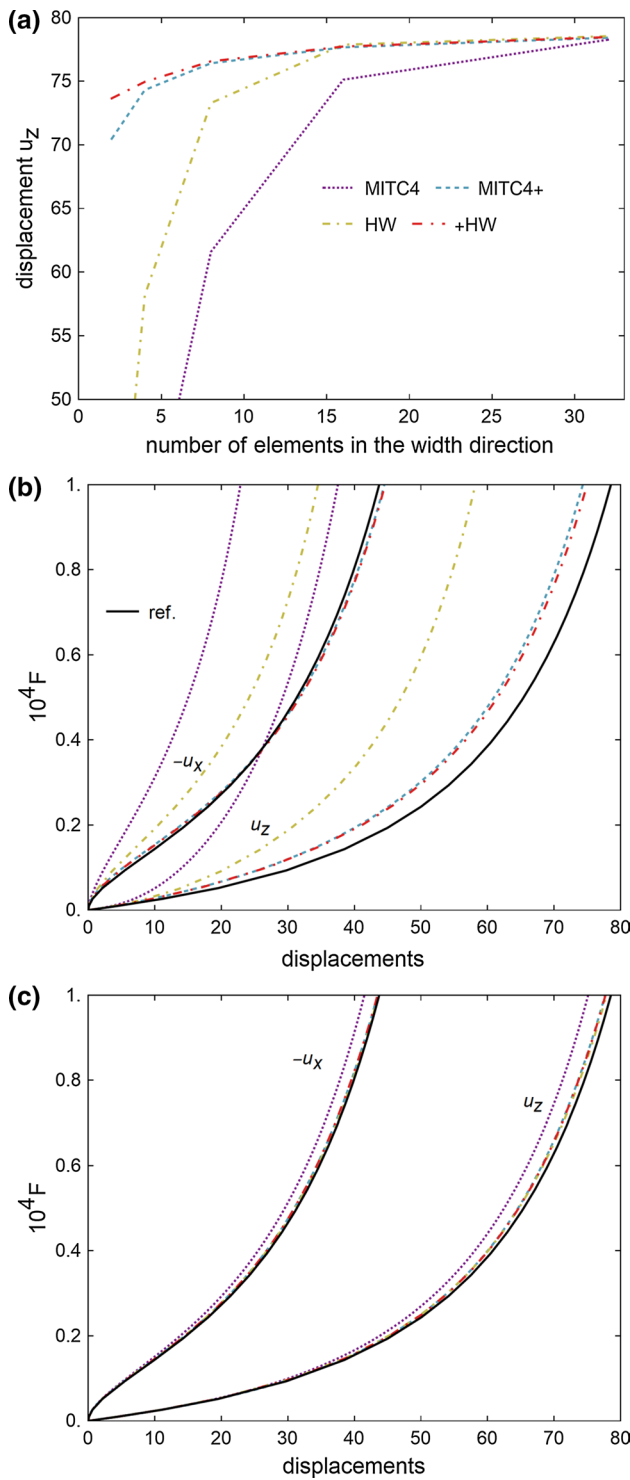


**Fig. 12** Raasch's hook, regular mesh: **a** convergence, **b**  $N=4$  mesh, **c**  $N=16$  mesh

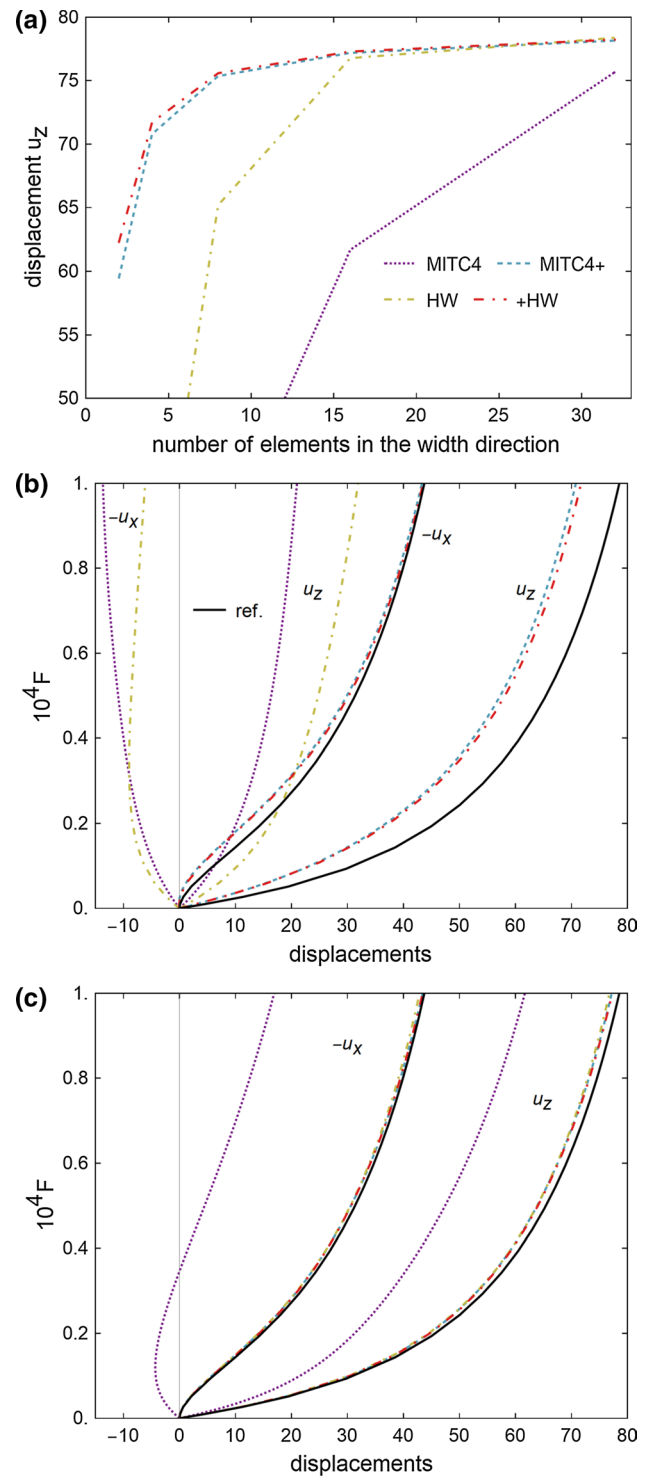


**Fig. 13** Raasch's hook, distorted mesh: **a** convergence, **b**  $N=4$  mesh, **c**  $N=16$  mesh

in Fig. 11. The ratio between the longest and the shortest element edge (in the curvilinear direction)  $L_{max}/L_{min}$  was set to 1.5 and 2 for the first and the second arch, respectively. This is a demanding test for distorted meshes. The single curved

shell exhibits membrane-bending deformations (large bending is followed by stiffer membrane response).

Figures 12a and 13a show convergence for displacement  $u_z$  at point A for  $F = 10^{-4}$ . The computed converged

**Table 5** Raasch’s hook: computational details for  $F_z = 10^{-4}$  and  $N=16$  for regular mesh (top) and distorted mesh (bottom)

FE	MITC4	MITC4+ [14]	HW [25]	+HW
Displacement $u_z$ ( $\frac{u_z}{u_{z,ref}}$ [%])	75.12 (96)	77.66 (99)	77.87 (99)	77.73 (99)
Normalized CPU time	1.00	1.13	0.18	0.22
Req. no. of load increments	92	96	22	22
Total number of iterations	883	930	120	124
Number of back-steps	3	4	0	0
Displacement $u_z$ ( $\frac{u_z}{u_{z,ref}}$ [%])	61.68 (79)	77.19 (98)	76.77 (98)	77.29 (98)
Normalized CPU time	1.00	1.15	0.20	0.27
Req. no. of load increments	91	96	22	22
Total number of iterations	874	931	120	124
Number of back-steps	6	4	0	0

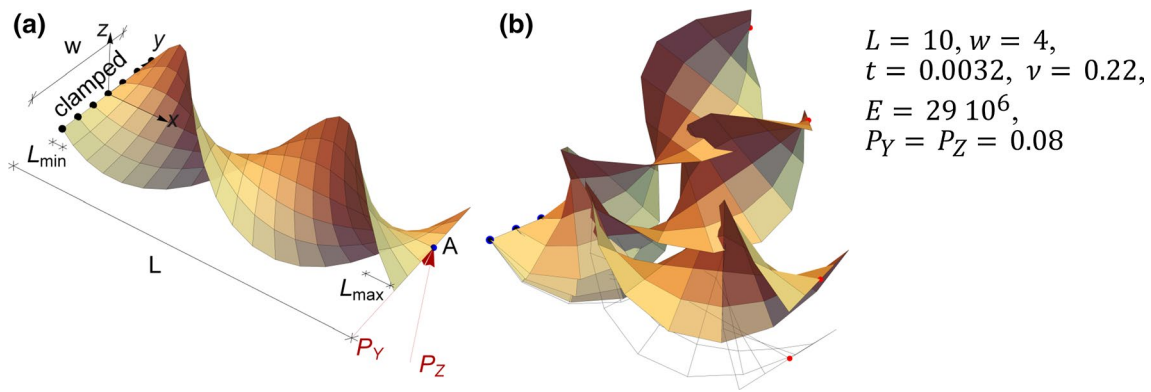


**Fig. 14** Twisted beam: **a** problem data and distorted mesh; **b** initial and three deformed configurations for +HW (regular mesh)

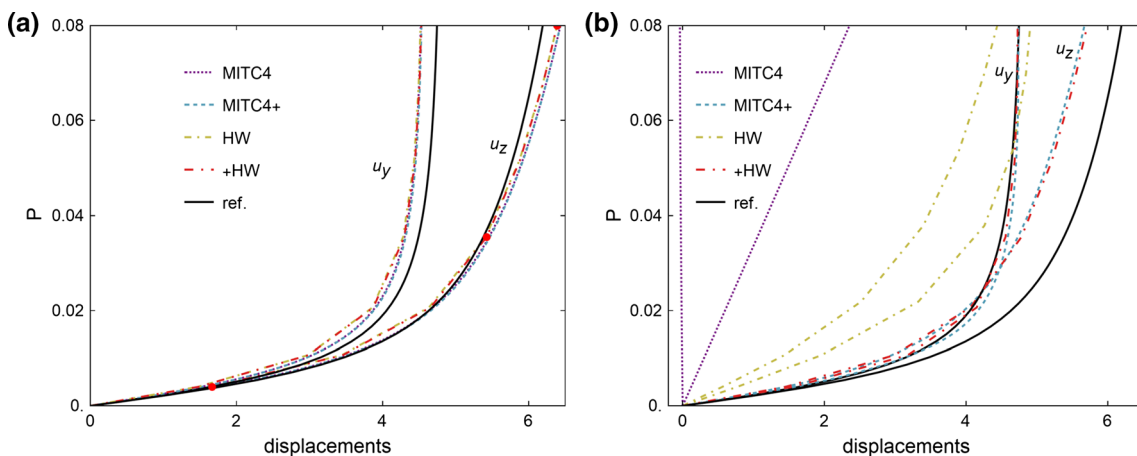


**Fig. 15** Twisted beam: load–displacement curves for **a** regular mesh and **b** distorted mesh. Red dots mark deformed configurations in Fig. 14b

solution,  $u_{z,ref} = 78.55$ , was reached by all formulations for regular mesh but not for distorted mesh. The differences are large.

Figures 12b, c and 13b, c present the applied force versus displacement at point A for two regular and two distorted meshes. As the reference result, we adopt the solution with

regular mesh of  $(64 + 96) \times 32$  HW elements that is in perfect agreement with that by  $8 \times 40$  MITC9 elements in [14]. MITC4+ and +HW are superior; they provide excellent agreement with the reference solution already for mesh with  $N=4$  and are almost insensitive to mesh distortion. MITC4 performs the poorest; it is far from the reference solution for

**Table 6** Twisted beam: computational details for  $P=0.08$  for regular mesh (top) and distorted mesh (bottom);  $u_{y,ref} = 4.75$

FE	MITC4	MITC4+ [14]	HW [25]	+HW
Displacement $u_y$ ( $\frac{u_y}{u_{y,ref}}$ [%])	4.52 (95)	4.53 (95)	4.52 (95)	4.53 (95)
Normalized CPU time	1.00	1.37	0.10	0.09
Req. no. of load increments	61	78	7	7
Total number of iterations	664	802	43	43
Number of back-steps	10	14	0	0
Displacement $u_y$ ( $\frac{u_y}{u_{y,ref}}$ [%])	-0.04 (-1)	4.74 (100)	4.91 (103)	4.73 (100)
Normalized CPU time	1.00	13.5	0.93	1.71
Req. no. of load increments	7	56	7	7
Total number of iterations	51	585	41	43
Number of back-steps	0	9	0	0

the mesh with  $N=4$  and it shows significant mesh-distortion sensitivity. It does not get near to the reference solution, even for fine distorted mesh, see Fig. 13c. HW performs a little better than MITC4; it is quite sensitive to mesh distortion, but it reaches the reference solution for finer distorted mesh, see Fig. 13c. Table 5 compares the robustness and speed of the formulations.

### 4.6 Twisted beam

We consider a version of the twisted beam-like shell problem considered in e.g. [14, 15, 26]. The beam is clamped at one edge and subjected to two forces,  $P = \lambda P_y = \lambda P_z$ , at the opposite end. The twist is  $2\pi$ . The shell undergoes considerable bending, which is followed by stretching, see Fig. 14b. Thus, this is a test for membrane-bending shell behavior.

In Fig. 15, displacements  $u_z$  and  $u_y$  of point A are shown versus  $P$ ; reference results were obtained by regular mesh of  $20 \times 60$  HW elements. Regular and distorted meshes were used, with  $12 \times 4$  and  $6 \times 20$  elements, respectively; and ratio  $L_{min}/L_{max} = 1/2$ , see Fig. 14a. Despite a coarse regular

mesh, there is almost no difference in response between the formulations, which match well the reference results, see Fig. 15a. Mesh distortion, see Fig. 15b, affects MITC4 greatly (the results are far from the reference solution and useless), the HW solution is affected considerably, while MITC4+ and +HW show incredibly little sensitivity to mesh distortion. Table 6 shows that HW and +HW are the fastest, do not require back-steps, and take large load increments.

The twisted beam was also chosen to check for a possible undesirable hysteresis because of the configuration dependent weighting factors (20) applied in MITC4+ and +HW. We chose the twist of  $\pi/8$  and distorted mesh with ratio  $L_{max}/L_{min} = 4$ ; see Fig. 16. The uniformly distributed load  $P = \lambda P_x$  was increased until  $\lambda = 1$ , which produced large membrane strains, and then decreased to  $P = 0$ . Figure 16 shows no hysteresis effect, which confirms that the weighting factors in (20) were carefully calibrated.

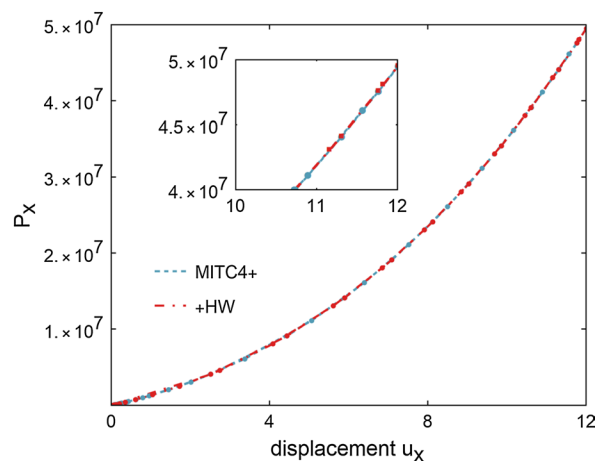
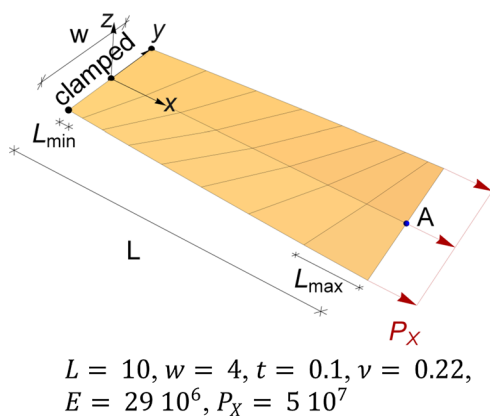


**Fig. 16** Beam with the twist of  $\pi/8$

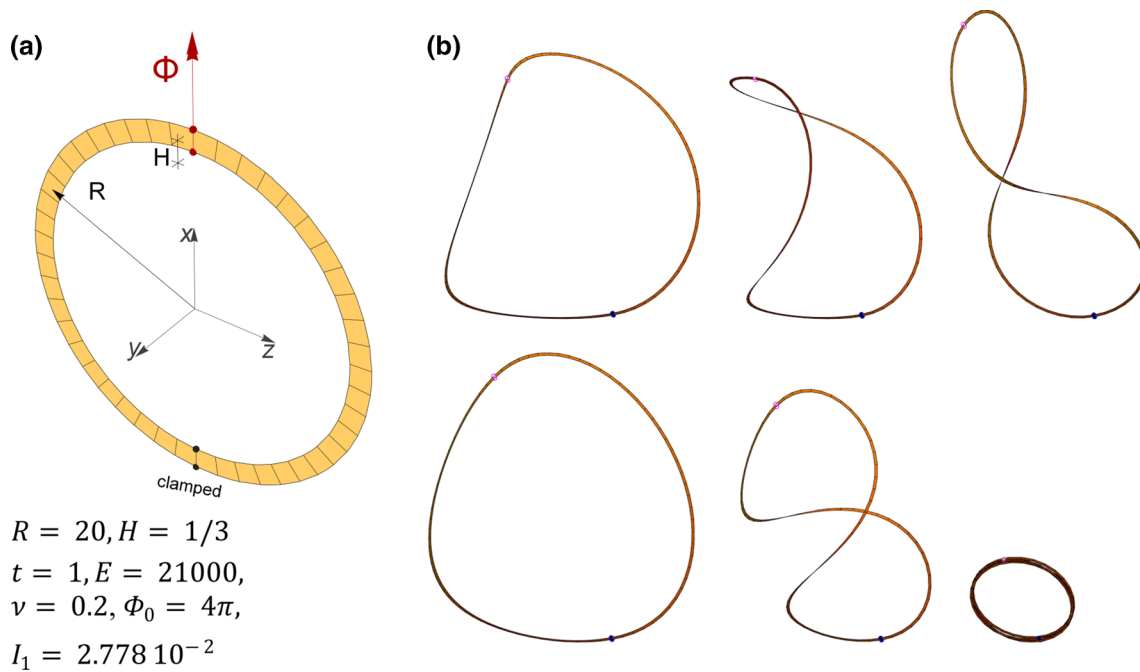


**Fig. 17** Deployable ring: **a** problem data; **b**  $80 \times 1$  mesh; deformed configurations at points marked in Fig. 18 for MITC4 (top) and for +HW (bottom)

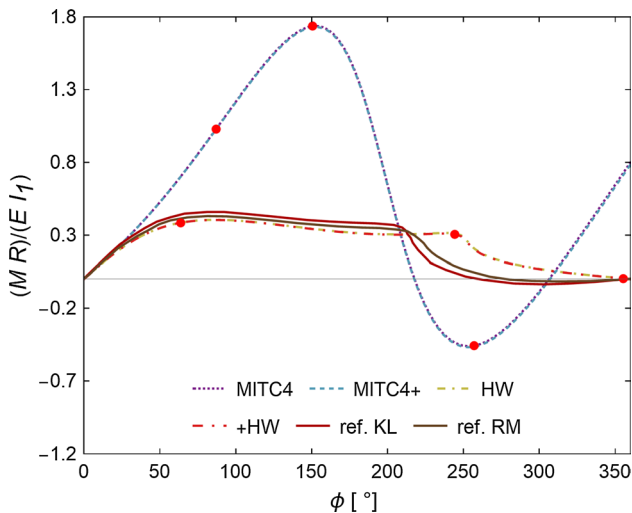


**Fig. 18** Deployable ring: load–displacement curves for  $80 \times 1$  mesh; red dots mark deformed configurations in Fig. 17b

### 4.7 Deployable ring

The deployable ring example, see Fig. 17a, was studied in detail in [8]. It was recomputed by isogeometric Reissner–Mindlin (RM) and Kirchhoff–Love (KL) shell formulations in [19]. The ring is clamped along the bottom

cross-section and subjected to imposed rotation  $\Phi = \lambda \Phi_0$  along the top cross-section. We used meshes of  $80 \times 1$ ,  $1200 \times 1$  and  $1200 \times 4$  elements. Because our formulations do not have drilling rotation, the meshes were in the ring’s plane. This is in contrast to the mentioned isogeometric computations in [19], where the elements were oriented perpendicular to the ring’s plane and drilling rotation was applied. For this reason, our results do not match closely the ones from [19]. According to [8], at  $\Phi = 2\pi$ , the ring deploys into three circles with a radius  $R/3$ , and its initial shape is regained at  $\Phi = 4\pi$ . The example is a test for coupling of bending and twisting, with large parts of ring exhibiting almost rigid-body motion.

The results are given in Figs. 18 and 19, where moment-rotation curves are shown;  $M$  is the sum of reactions at nodes with imposed rotation. Figure 18 shows that MITC4 and MITC4+ exhibit severe membrane locking for the coarser mesh and predict completely deviating solution. It seems that the solution is non-physical, because at  $\Phi \approx 2\pi$  the elements cross each other, see Fig. 17b. The present ANS membrane treatment has no effect for this example, because MITC4 and MITC4+ behave in the same way.

The HW and +HW formulations predict solutions that are qualitatively close to those presented in [8, 19] and their results change only slightly with mesh refinement. For the  $1200 \times 1$  mesh, the results of all formulations almost coincide; however, MITC4 and MITC4+ fail to converge at  $\Phi \approx 2.6\pi$ , see Fig. 19a. For the  $1200 \times 4$  mesh, the

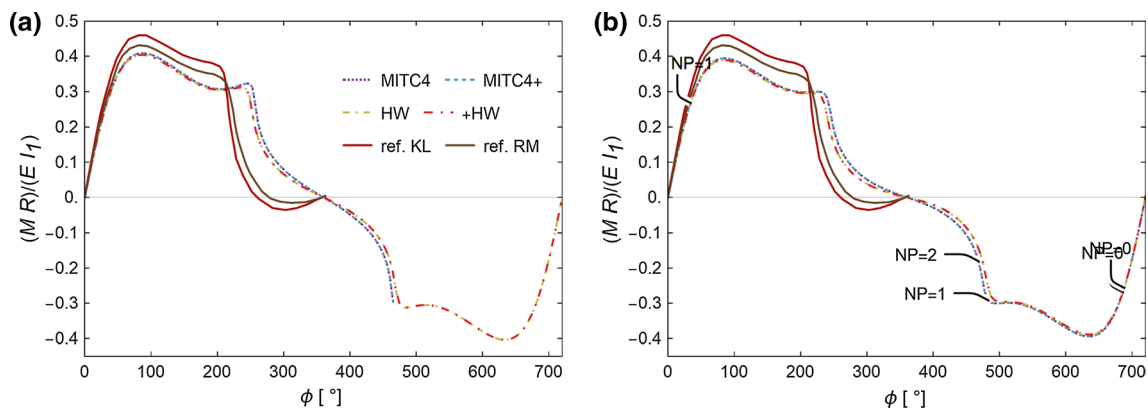


**Fig. 19** Deployable ring: load–displacement curves for **a**  $1200 \times 1$  and **b**  $1200 \times 4$  mesh

formulations provide the same response up to the final rotation  $\Phi = 4\pi$ , see Fig. 19b. In Fig. 19b, we show the number of negative pivots (NP) on the solution path; a change on NP indicates the occurrence of critical (i.e. limit or bifurcation) point. It is interesting that the formulations do not predict critical points at the same configurations; moreover, MITC4 and MITC4+ detect two more than HW and +HW.

### 5 Conclusions

It is now understood theoretically (see e.g. [18]) and has been confirmed by numerical experiments (see, e.g., [25] and the examples in this work) that the use of (hybrid-)mixed formulations is essential to get finite elements that allow for large solution steps. Unfortunately, the hybrid-mixed shell finite element formulations do not completely remove membrane and transverse shear locking. It was shown in [25] that it is possible to cure the transverse-shear locking in hybrid-mixed shell element by applying the ANS interpolations on the top of the Hu–Washizu interpolations for the stress resultants and strains. However, such hybrid-mixed shell element still remains sensitive to membrane locking for distorted meshes as has been clearly shown by our numerical examples. On the other hand, the same numerical examples have demonstrated that the mesh distortion sensitivity can be effectively reduced by assumed natural strain interpolation of membrane strains, in particular by the recent version derived in [14].

For these reasons, we have combined the Hu–Washizu element with the ANS shear strains from [25] with the ANS interpolations for the membrane strains from [14]. The result is a novel element, which is low-sensitive to mesh distortion and allows for large solution steps. Although the difference between our element and the one from [25] may seem to be small, the effects in numerical results are far from small and very beneficial. This has been clearly demonstrated by a set

of representative numerical examples, which were carefully chosen to model various types of deformation states in (thin) shells.

The low sensitivity to mesh distortions for elements with ANS interpolation of membrane strains is basically due to the geometric parameters, which act as weighting factors and change in each converged configuration. They weight membrane strains in the pre-selected points (that are always coplanar) according to the current element’s distortion. The weighting factors are well calibrated, so that no side effects, like a hysteresis, appear.

For the theoretical discussion on ability of mixed formulations to take large solution steps, we refer to [18]. In [18], this issue is discussed for nonlinear mixed solid finite elements and Hellinger–Reissner (HR) functional, but the conclusions are applicable also for the Hu–Washizu functional and shell finite elements. The main conclusion in [18] is that for mixed HR elements, the tangent stiffness matrix in the current iteration is much closer to the secant stiffness matrix of the current increment (than for the displacement-based elements). The reason is better iterative approximation of the converged incremental stresses. As a consequence, mixed formulations allow for larger solution steps and smaller number of iterations in comparison with the displacement-based formulations.

The presented work can be seen as a step towards the optimal low order (4-node) shell nonlinear finite element (that is based on classical shell theory with transverse shear effects). In our opinion, the classical-theory-based optimal nonlinear shell finite element is of great practical interest and thus worth investigating.

### References

1. Bathe KJ (2014) Finite element procedures, 2 edn. K.J. Bathe, Watertown, MA

2. Brank B, Ibrahimbegovic A (2001) On the relation between different parametrizations of finite rotations for shells. *Eng Comput* 18:950–973
3. Brank B, Perić D, Damjanić FB (1997) On large deformations of thin elasto-plastic shells: Implementation of a finite rotation model for quadrilateral shell element. *Int J Numer Methods Eng* 40:689–726
4. Choi CK, Paik JG (1996) An effective four node degenerated shell element for geometrically nonlinear analysis. *Thin-Walled Struct* 24(3):261–283
5. Crisfield MA (1996) *Non-linear finite element analysis of solids and structures, volume 2: advanced topics*. Wiley, Hoboken
6. Dujc J, Brank B (2012) Stress resultant plasticity for shells revisited. *Comput Methods Appl Mech Eng* 247:146–165
7. Dvorkin EN, Bathe KJ (1984) A continuum mechanics based four-node shell element for general nonlinear analysis. *Eng Comput* 1:77–88
8. Goto Y, Watanabe Y, Kasugai T, Obata M (1992) Elastic buckling phenomenon applicable to deployable rings. *Int J Solids Struct* 29(7):893–909
9. Gruttmann F, Wagner W (2005) A linear quadrilateral shell element with fast stiffness computation. *Comput Methods Appl Mech Eng* 194:4279–4300
10. Gruttmann F, Wagner W (2006) Structural analysis of composite laminates using a mixed hybrid shell element. *Comput Mech* 37:479–497
11. Ibrahimbegović A, Brank B, Courtois P (2001) Stress resultant geometrically exact form of classical shell model and vector-like parameterization of constrained finite rotations. *Int J Numer Methods Eng* 52(11):1235–1252
12. Ibrahimbegović A (2009) *Nonlinear solid mechanics*. Springer, Dordrecht
13. Ko Y, Lee PS, Bathe KJ (2017) A new MITC4+ shell element. *Comput Struct* 182:404–418
14. Ko Y, Lee PS, Bathe KJ (2017) The MITC4+ shell element in geometric nonlinear analysis. *Comput Struct* 185:1–14
15. Ko Y, Lee Y, Lee PS, Bathe KJ (2017) Performance of the MITC3+ and MITC4+ shell elements in widely-used benchmark problems. *Comput Struct* 193:187–206
16. Korelc J, Wriggers P (2016) *Automation of finite element methods*. Springer, Berlin
17. Kulikov GM, Plotnikova SV (2010) A family of ANS four-node exact geometry shell elements in general convected curvilinear coordinates. *Int J Numer Methods Eng* 83(10):1376–1406
18. Magisano D, Leonetti L, Garcea G (2017) Advantages of the mixed format in geometrically nonlinear analysis of beams and shells using solid finite elements. *Int J Numer Methods Eng* 109:1237–1262
19. Oesterle B, Sachse R, Ramm E, Bischoff M (2017) Hierarchic isogeometric large rotation shell elements including linearized transverse shear parametrization. *Comput Methods Appl Mech Eng* 321:383–405
20. Pian THH, Sumihara K (1984) Rational approach for assumed stress finite elements. *Int J Numer Methods Eng* 20(9):1685–1695
21. Simo JC, Armero F (1992) Geometrically non-linear enhanced strain mixed methods and the method of incompatible modes. *Int J Numer Methods Eng* 33(7):1413–1449
22. Simo JC, Fox DD (1989) On a stress resultant geometrically exact shell model. Part I: formulation and optimal parametrization. *Comput Methods Appl Mech Eng* 72:267–304
23. Simo JC, Fox DD, Rifai MS (1990) On a stress resultant geometrically exact shell model. Part III: computational aspects of the nonlinear theory. *Comput Methods Appl Mech Eng* 79:21–70
24. Simo JC, Hughes TJR (1986) On the variational foundations of assumed strain methods. *J Appl Mech* 53(1):51–54
25. Wagner W, Gruttmann F (2005) A robust non-linear mixed hybrid quadrilateral shell element. *Int J Numer Methods Eng* 64:635–666
26. Wiśniewski K (2010) *Finite rotation shells, basic equations and finite elements for Reissner kinematics*. Springer, Dordrecht
27. Wisniewski K, Turska E (2009) Improved 4-node Hu–Washizu elements based on skew coordinates. *Comput Struct* 87:407–424
28. Wisniewski K, Wagner W, Turska E, Gruttmann F (2010) Four-node Hu–Washizu elements based on skew coordinates and contravariant assumed strain. *Comput Struct* 88:1278–1284
29. Wriggers P (2008) *Nonlinear finite element methods*. Springer, New York
30. Yu G, Xie X, Carstensen C (2011) Uniform convergence and a posteriori error estimation for assumed stress hybrid finite element methods. *Comput Methods Appl Mech Eng* 200:2421–2433

**Publisher's Note** Springer Nature remains neutral with regard to jurisdictional claims in published maps and institutional affiliations.